ACS OMEGA

Open Access

This article is licensed under CC-BY-NC-ND 4.0

http://pubs.acs.org/journal/acsodf

Article

Optimization of Laser-Wavelength Dependence for Open-Air Atmospheric Pressure Pulsed Laser Deposition of AlCrFeMnTi High-Entropy Alloy for Tailored Surface Properties

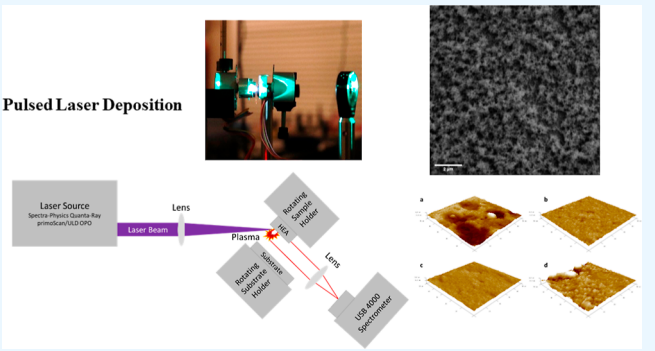
Hossein Mahdavi, Armin Asghari Alamdari, Abdullah Kepceoğlu, M. Barış Yağcı, Uğur Ünal, and Hadi Jahangiri*

Cite This: *ACS Omega* 2024, 9, 22495−22505

Read Online

ACCESS | Metrics & More | Article Recommendations | Supporting Information

ABSTRACT: High-entropy alloys (HEAs) have garnered significant attention in different fields due to their exceptional mechanical and physical properties, making them promising candidates for various applications. Several techniques, including physical vapor deposition and pulsed laser deposition (PLD), have been employed for the fabrication of HEA thin films. In this study, we explore a novel approach to synthesizing the lightweight HEA (LWHEA) AlCrFeMnTi using PLD in air at atmospheric pressure with a particular focus on the influence of the laser wavelength on the deposition process and the resulting alloy characteristics. This research investigates the impact of different laser wavelengths on the LWHEA's characterization and the optimization of laser wavelength dependence in air at atmospheric pressure PLD of LWHEA AlCrFeMnTi for tailored surface properties such as phase composition, microstructure, and corrosion resistance. Systematically varying the laser wavelength was attempted to optimize the deposition conditions. This was aimed at achieving enhanced properties and precise control over the alloy's composition. This work contributes to a deeper understanding of the open air PLD process for LWHEAs and sheds light on the role of the laser wavelength in tailoring their properties, which can have significant implications for the development of advanced materials for aerospace, automotive, and other high-performance applications. Ultimately, this research aims to provide valuable insights into the design and fabrication of LWHEAs with tailored properties through laser-based deposition techniques.



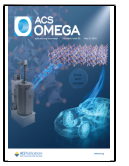
Downloaded via KOC UNIV on January 2, 2025 at 06:40:56 (UTC).
See https://pubs.acs.org/sharingguidelines for options on how to legitimately share published articles.

1. INTRODUCTION

Oxide ceramics offer a wide range of properties due to their diverse and adjustable structure, including crystallography, microstructure, and electron density.[1,2] Recent advancements in oxide structure design have focused on engineering configurational entropy, enabling the creation of complex multicomponent oxides known as high-entropy oxides (HEOs).[3,4] These oxides, consisting of five or more oxide components with equimolar or near-equimolar compositions or an atomic concentration between 5 and 35%,[5] form solid solutions with randomly distributed cations on a cation sublattice.[3,4] HEOs exhibit tolerance for cation multivalency and vacancies, allowing for tailored lattice distortion, oxygen stoichiometry, and superior properties.[6] Additionally, there is increasing research on thin film deposition of high-entropy alloys (HEAs) and HEOs using techniques like DC and RF sputtering, focusing on mechanical, structural, electrical, and magnetic properties.[7−13] These materials find applications in high-tech industries, offering exceptional protection and properties such as improved wear resistance, corrosion resistance, and high hardness.[1]

Pulsed laser deposition (PLD) is a widely employed technique for the deposition of thin films, offering advantages such as compatibility with compounds and alloys, including low vapor pressure materials.[11,12] Briefly, during PLD, the pulsed laser source is focused on the HEA target, usually prepared through a mechanical alloying (MA)/sintering process at high temperatures and high pressures, causing the evaporation and subsequent condensation on the surface of the desired substrate.[14] The PLD technique is intrinsically flexible and versatile and allows the deposition of high-quality films on low-temperature substrates.[14] The characteristics of the deposited thin films via PLD depend on several parameters such as substrate temperature, ambient oxygen pressure, laser

Received: April 4, 2024
Revised: April 15, 2024
Accepted: April 17, 2024
Published: May 8, 2024



© 2024 The Authors. Published by American Chemical Society

Table 1. Nominal and Actual Compositions of the Target (wt % and at. %)

	Al		Cr		Fe		Mn		Ti	
	wt %	at. %	wt %	at. %	wt %	at. %	wt %	at. %	wt %	at. %
nominal	11.35	20.00	21.88	20.00	23.50	20.00	23.12	20.00	20.15	20.00
actual	11.33	19.95	21.79	19.92	23.56	20.05	23.25	20.11	20.07	19.97

intensity, and so forth. Unlike sputter-deposition, PLD enables higher instantaneous deposition rates and the delivery of species with greater energy. Thin-film deposition differs significantly from bulk material production, providing an opportunity to generate HEA and HEO films with distinct properties.[15] Due to the myriad advantages of the PLD technique for the deposition of thin films, the technique has been employed for the fabrication of high-entropy materials in several different applications. Guo et al. developed a nanoporous HEO with a composition of $(Co_{0.2}Ni_{0.2}Cu_{0.2}Mg_{0.2}Zn_{0.2})O$ and, by varying the laser energy fluence, investigating the morphology of the HEO thin film.[16] Laszlo et al. studied the mechanical properties of pulsed laser-deposited $AlCoCrFeNi_x$ HEAs and nitrides[11] and also explored the biocorrosion behavior of the thin-film alloys in simulated body fluid.[17] In another work, Jung et al. employed PLD for the fabrication of superconductive thin films of TaNbHfZrTi HEA on c-cut Al_2O_3 substrates over a wide range of temperatures.[18] Laser deposition in open air at atmospheric pressure is a low-cost and facile method of thin-film fabrication because as opposed to the conventional PLD technique, there is no requirement for the use of a vacuum chamber.[19] Open-air PLD has been employed in the fabrication of porous metal oxide films, such as nanoporous TiO_2 and ZnO.[19,20] Considering the merits of a facile process and low-cost fabrication, open-air PLD is a promising technique for preparing porous HEOs, which has not been explored to date.

In this work, open-air PLD was utilized for the deposition of AlCrFeMnTi, a lightweight HEA (LWHEA), onto a fluorine-doped tin oxide (FTO) substrate for the first time. The LWHEA targets were prepared through two-step MA and spark plasma sintering (SPS). PLD was carried out at four different pulsed laser wavelengths ranging from 320 to 350 nm. Surface characterization techniques, including scanning electron microscopy (SEM), transmission electron microscopy (TEM), atomic force microscopy (AFM), X-ray photoelectron spectroscopy (XPS), X-ray diffraction (XRD), potentiodynamic polarization, and electrochemical impedance spectroscopy (EIS), were employed to obtain the optimum PLD wavelength for further applications in mechanical, energy, and biomedical fields.

2. EXPERIMENTAL SECTION

In this research, a thin film of AlCrFeMnTi was deposited onto a substrate of FTO using the PLD technique. The LWHEA AlCrFeMnTi target was produced by MA and consolidated by SPS. The nominal and actual produced target composition was measured by XRF, and the results are presented in Table 1.

A Q-switched Nd:YAG laser with a built-in single pass amplifier (Spectra-Physics Quanta-Ray) was utilized for the deposition process. To generate the required laser energy, an OPO laser (Spectra-Physics primoScan/ULD) was employed, operating at various wavelengths including 320, 330, 340, and 350 nm. The laser operated at a repetition rate of 10 Hz and had an approximate laser pulse energy of 20 mJ. To ensure precise targeting of the laser beam, a 7 cm focal length planoconvex lens was used to focus the laser beam onto the target material. The experimental setup, schematics, counter rotating motors, focusing lens, and produced plasma are shown in Figure 1. The FTO substrate was positioned 8 mm from the

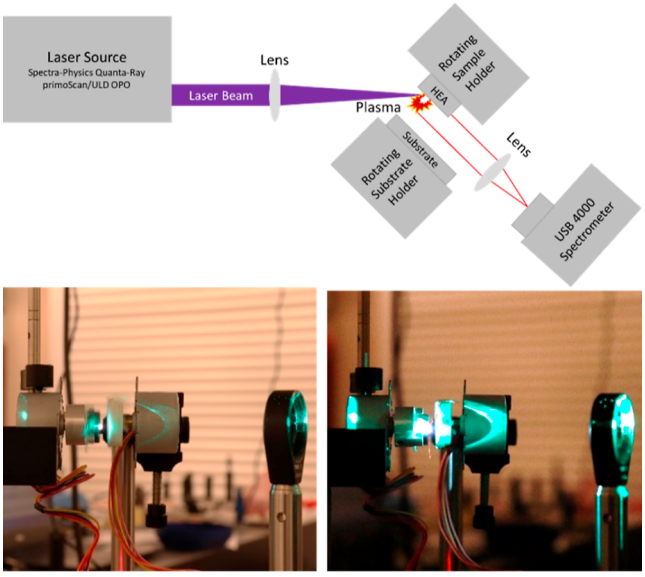


Figure 1. Experimental setup, schematics, counter-rotating motors, focusing lens, and produced plasma.

target. Both of the target and substrate were fixed to a rotating holder. Additionally, an angle of 45° was set between the laser beam and the target surface to optimize the deposition process. To characterize the laser-induced plasma during the deposition, a fiber-coupled miniature CCD spectrometer (Ocean Optics, USB4000-VIS-NIR) was employed to perform laser-induced breakdown spectroscopy (LIBS) measurements. This spectrometer allowed for the collection and analysis of spectral data from plasma generated by the laser interaction with the target material. Microstructural analysis of the deposited film was conducted using a Carl Zeiss Ultra Plus field emission SEM system with both secondary and backscattered electron detectors. The microstructure and crystallinity of the samples and the constituent elements distribution was investigated with high resolution transmission electron microscopy (HETEM, Hitachi, HF5000). Phase identification of the mechanically alloyed powder and the as-sintered sample was performed by analyzing XRD patterns obtained from a Bruker D2 ADVANCE X-ray diffractometer utilizing a Cu radiation target (λ = 1.5405 Å). The surface topography of the deposited film was examined by using AFM in tapping mode, employing a Bruker Dimension Icon instrument. Additionally, the optical properties of the film were investigated through absorption/reflection spectra measurements by using a Shimadzu UV−Vis−NIR 3600 spectrophotometer. The comprehensive characterization of the AlCrFeMnTi film provides valuable insights into its microstructure, phase composition, surface topography, and optical behavior. Moreover, XPS with a

https://doi.org/10.1021/acsomega.4c03245
ACS Omega 2024, 9, 22495−22505

Thermo Scientific K-Alpha instrument, utilizing an Al Kα monochromator source at 1486.6 eV, was employed to determine the surface composition and oxidation states. All XPS spectra were corrected based on the binding energy (BE) of C 1s = 284.50 eV. Electrochemical measurements for corrosion assessments were carried out using a conventional three-electrode setup, consisting of PLD-coated FTO as the working electrode, a graphite rod as the counter electrode, and Hg/HgO as the reference electrode, connected to a BioLogic VSP Potentiostat. Phosphate buffer solution with a pH of 7.4 was utilized for all of the electrochemical experiments.

3. RESULTS AND DISCUSSION

LIBS was employed to investigate the elemental emission peaks of the AlCrFeMnTi LWHEA. Additionally, individual LIBS emission spectra were collected from pellets prepared using each element (Al, Cr, Fe, Mn, and Ti), as depicted in Figure 2. The LIBS analysis of the AlCrFeMnTi LWHEA yielded valuable insights into its elemental emission peaks, shedding light on its composition. In the initial stage, individual disks were created from each component of the AlCrFeMnTi LWHEA, as illustrated in Figure S1. These disks served as targets for LIBS analysis references. LIBS spectra were obtained for each component of the AlCrFeMnTi LWHEA, along with the LIBS spectra of air, all cross-validated against the LIBS spectra of the mechanically alloyed and SPS-assembled target. The spectra revealed detected peaks for all elemental components in the LWHEA. The obtained spectral data were compared with the National Institute of Standards and Technology (NIST) atomic spectra database to precisely identify emission peaks and to illuminate the alloy's composition and spectroscopic properties.

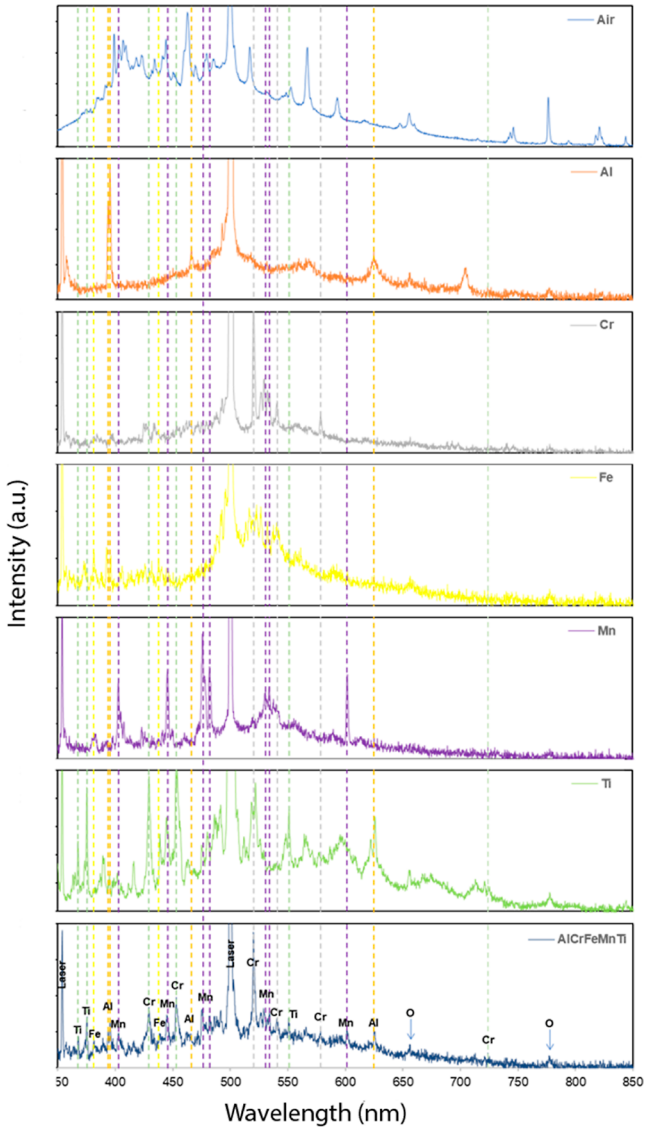


Figure 2. LIBS spectra of the LWHEA (AlCrFeMnTi) and metal component pellets as the used target.

The LIBS analysis of the AlCrFeMnTi alloy unveiled characteristic emission peaks indicative of its elemental constituents. Between 393 and 396 nm, a double peak corresponding to Al I was observed, while additional peaks at 466 and 625 nm indicated the presence of Al II.[21] These findings reveal the coexistence of neutral (Al I) and single ionized (Al II) aluminum atoms in the alloy's plasma. In the case of chromium (Cr), distinct emission peaks were identified in the LIBS spectrum at wavelengths of 429, 453, 520, 540, and 724 nm, corresponding to Cr I. These spectral features provide valuable information about the presence and ionization state of chromium in the sample.[22] For iron (Fe), emission peaks at 381 and 438 nm were observed in the LIBS spectrum, signifying the presence of single ionized iron atoms within the plasma.[21] Manganese (Mn) emission peaks were also evident in the LIBS spectrum at 403, 445, and 476 nm, representing Mn I, while double peaks at 530 and 524 nm pointed at the presence of single ionized manganese (Mn II) atoms. These spectral features enable the identification of both Mn I and Mn II in the alloy.[21] Regarding titanium (Ti), emission peaks around 368, 375, and 550 nm were observed in the LIBS spectrum. However, due to the limited resolving power of the LIBS spectrometer, it was challenging to distinguish between emission from Ti I and Ti II ions.[23] Further investigations employing higher-resolution spectrometers may be required to resolve this ambiguity accurately. In addition to the observations of elemental emission peaks from the AlCrFeMnTi LWHEA, we also detected the presence of oxygen atom peaks at 655 and 776 nm in the LIBS spectrum.[24] These observations suggest that, apart from laser ablation of the target material, oxygen ions were also generated within the plasma.[25]

Figure 3a presents TEM-EDS images illustrating the deposited film of LWHEA AlCrFeMnTi prepared using PLD. In Figure 3b–g, the results of TEM-EDS element mapping offer valuable insights into the composition distribution within the coated film. Evidently, all constituent elements exhibit a uniform distribution throughout the sample, aligning with the findings in LIBS spectra analysis.[26,27] It is noteworthy that in addition to the primary elements, oxygen was also detected on the coated film's surface. This observation implies that during the PLD process conducted in an open-air environment, a portion or the entirety of the film composition underwent oxidation. This phenomenon highlights the significance of environmental conditions during PLD as they can influence the film's chemical composition and potentially impact its properties, making it essential to consider and control oxidation effects for precise film deposition in real-world applications.[28]

Figure 4 presents the XRD spectrum of the coated AlCrFeMnTi samples utilizing 320, 330, 340, and 350 nm laser wavelengths. The XRD spectra indicate that varying the

https://doi.org/10.1021/acsomega.4c03245
ACS Omega 2024, 9, 22495−22505

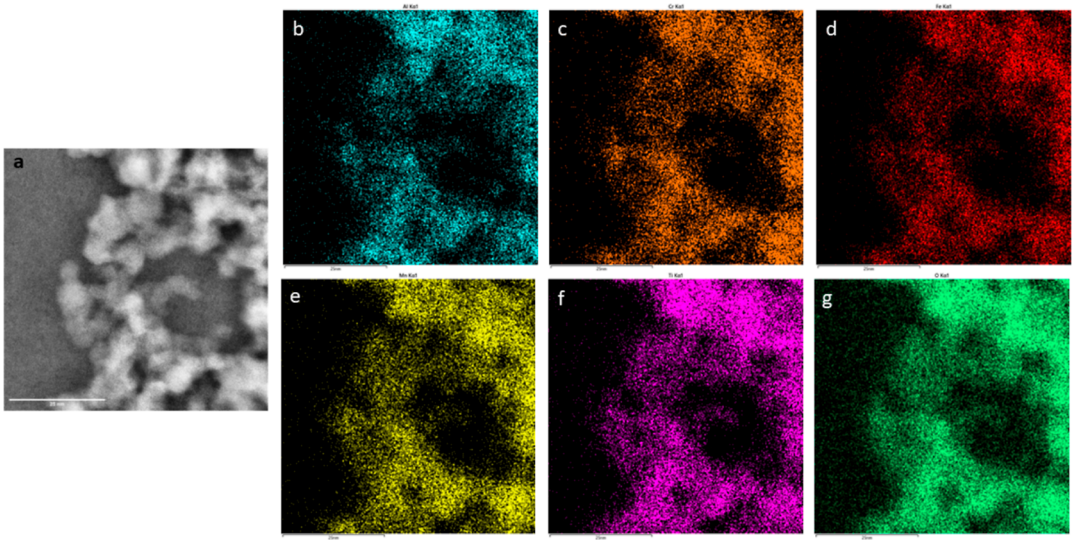


Figure 3. (a) TEM image and (b−g) TEM-EDS elemental mapping of the LWHEA AlCrFeMnTi deposited film by PLD for Al, Cr, Fe, Mn, Ti, and O, respectively.

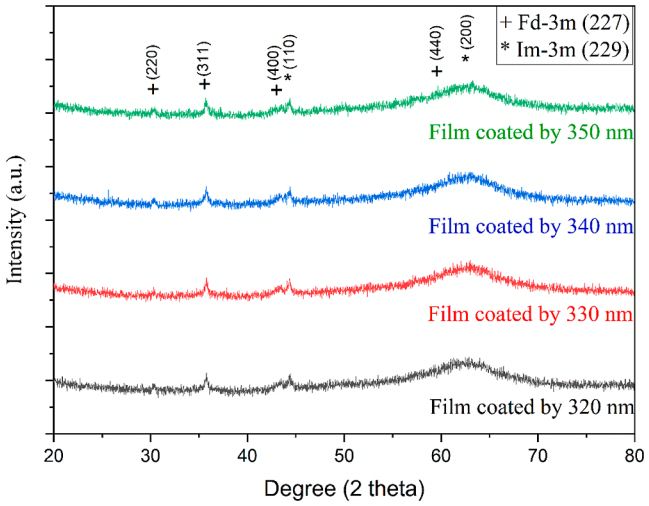


Figure 4. XRD spectrum of the LWHEA AlCrFeMnTi deposited film by PLD when employed at 320, 330, 340, and 350 nm wavelengths.

wavelength of the laser, while keeping the power constant, does not have any effect on the phases of the deposited film. The XRD analysis reveals that the coated LWHEA film exhibits a composite structure, comprising both amorphous and crystallized phases.[12,29] The calculated ratios indicate that the crystallized phase constitutes 17.57, 17.95, 18.51, and 17.96% of the film, while the amorphous phase ratio was calculated as 82.43, 82.05, 81.49, and 82.04% when using a laser with 320, 330, 340, and 350 nm wavelengths, respectively. Remarkably, the observed low peak intensity and broad full width at half-maximum (FWHM) values align well with the calculated values. While a LWHEA was employed as the target material during the PLD process, the open-air deposition environment led to the formation of a crystallized structure encompassing two distinct phases: a metallic phase in the $Im\bar{3}m$ (229) space group, BCC structure, and an oxide phase in the $Fd\bar{3}m$ (227) space group, FCC structure.[12,30] These findings are consistent with the results obtained from LIBS and the elemental mapping analysis (MAP-EDS) as the LIBS analysis also clearly detected ionic and metallic peaks in the spectra of metals, along with oxygen spectra. Utilizing the TOPAS software, the quantitative analysis determined that the metallic phase represents 43.25, 43.72, 43.84, and 43.90% of the film, while the oxide phase constitutes 56.75, 56.28, 56.16, and 56.10% when the laser was used at wavelengths of 320, 330, 340, and 350 nm, respectively. The XRD peaks corresponding to the metallic structure were observed at angles of 44.42 and 62.24°, while the peaks associated with the oxide phase were identified at angles of 30.27, 35.74, 43.26, and 60.05°.

The TEM-SAED pattern of the AlCrFeMnTi deposited film, generated by using 340 nm wavelength, corresponding to the film with the most intense XRD spectrum, is shown in Figure 5. In this pattern, two distinct phases are clearly visible: a metallic phase characterized by a BCC structure and an oxide

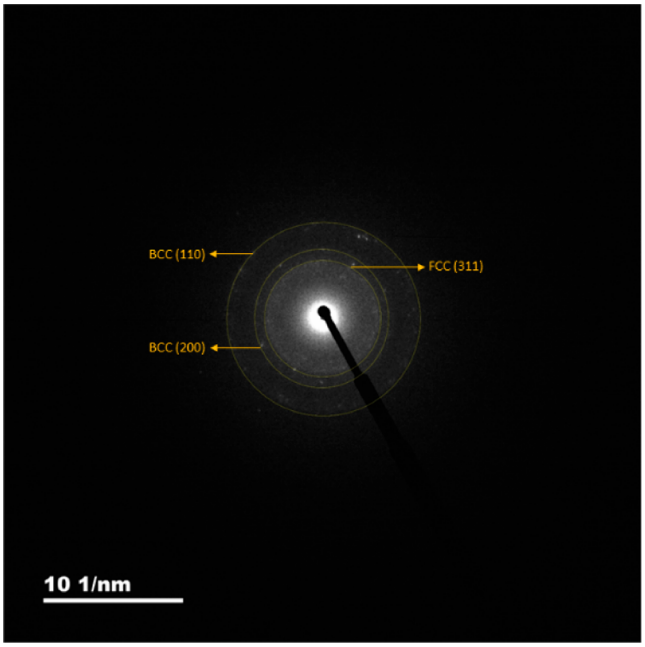


Figure 5. TEM-SAED pattern of the AlCrFeMnTi deposited film by PLD at 340 nm wavelength.

https://doi.org/10.1021/acsomega.4c03245
ACS Omega 2024, 9, 22495−22505

phase with an FCC structure. The BCC structure exhibits prominent (110) and (200) planes with the corresponding *d* values of 2.0433 and 1.4453 Å, while the FCC structure is represented by the (311) plane with a d value of 2.5091 Å. These findings reveal slight shifts in the d values, indicating lattice distortion in the LWHEA, as also observed in the XRD spectrum, aligning with the TEM-SAED results.

Figure 6 illustrates the SEM images corresponding to the deposition of an AlCrFeMnTi film on the FTO substrate using

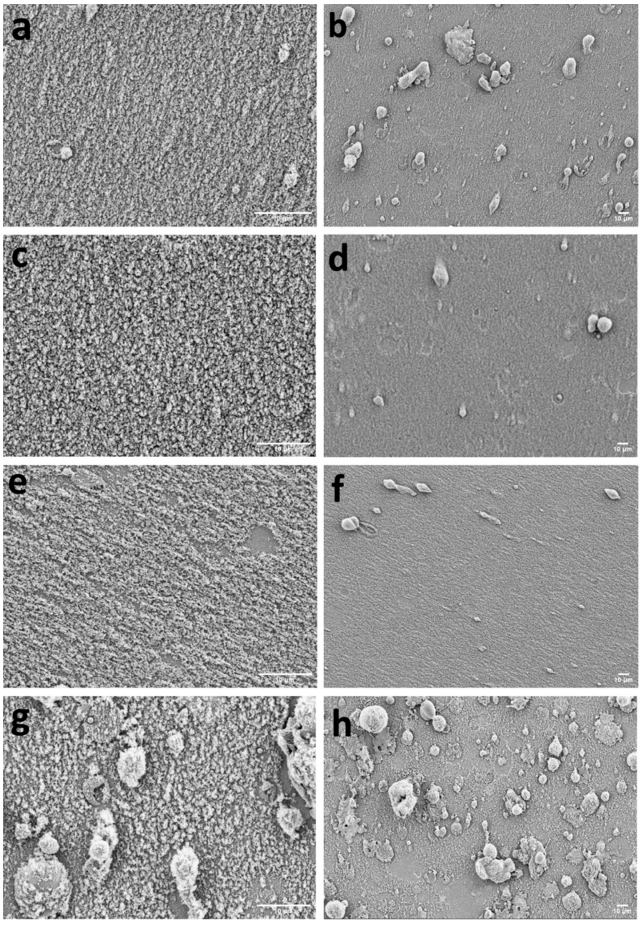


Figure 6. SEM micrographs of the deposited film of LWHEA AlCrFeMnTi by using the PLD method: (a,b) 320 nm wavelength, (c,d) 330 nm wavelength, (e,f) 340 nm wavelength, and (g,h) 350 nm wavelength.

laser beams with wavelengths of 320, 330, 340, and 350 nm while maintaining a fixed laser pulse energy of 20 mJ. The SEM images demonstrate that the film's morphology is influenced by the wavelength of the pulse laser, similar to that reported by Sanz et al.[31,32] Various wavelengths were used, resulting in a uniform coating across the entire surface. However, the size and quantity of the detached particles differ at different wavelengths. Based on the SEM analysis, the surfaces coated with 340 and 350 nm wavelengths exhibit the smoothest and roughest morphologies, respectively. At 340 nm, the number of detached particles is the lowest, and their size is below 10 μm, while the surfaces coated with a 350 nm laser wavelength have a higher number of detached particles, with sizes reaching up to 43 μm. The surfaces coated with 330 and 320 nm wavelengths also show detached particles, but the number and size of these particles fall between those observed at 350 and 340 nm.

Figure 7 displays a high-magnification SEM image of the AlCrFeMnTi deposited film produced using the PLD method

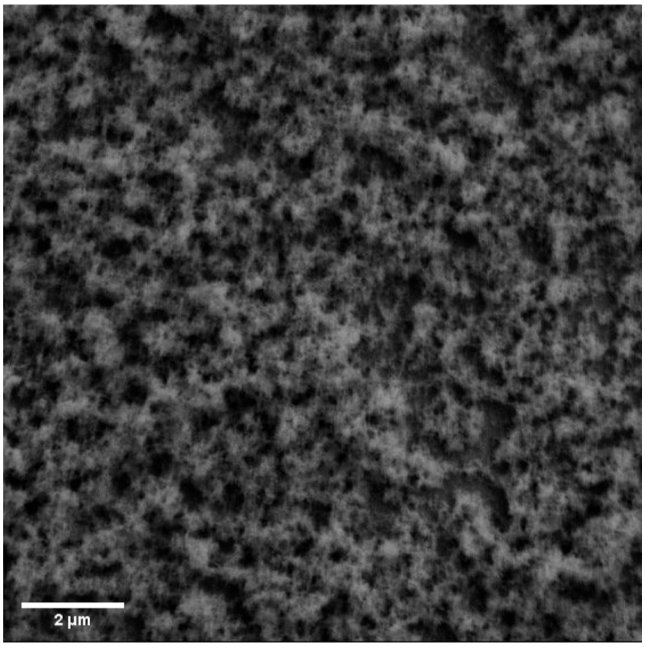


Figure 7. SEM micrograph of the LWHEA AlCrFeMnTi deposited by PLD with employed 340 nm wavelength.

with a 340 nm laser. SEM images of samples produced under atmospheric pressure and in an open-air environment reveal that the deposition process leads to the formation of complicated 3D nanostructures. These structures were highly porous and consist of accumulated nanoparticles, similar to the porous nanostructures reported by Sanz et al.[31,32] Laser ablation under ambient air pressure conditions results in the formation of complex and highly porous structures. Differences in the nanostructures produced with varying wavelengths can be attributed to distinct interactions between laser light and the materials involved.[31,32]

The AFM results of the deposited films of AlCrFeMnTi on silicon wafer by using PLD with various wavelengths (320, 330, 340, and 350 nm) are presented in Figure 8. AFM was employed to examine the surface topography and determine the root-mean-square (RMS) roughness values of the AlCrFeMnTi films. Figure 8 presents AFM images with dimensions of 50 × 50 μm^2 captured from the film surfaces. The investigation focused on the influence of the laser wavelength on the roughness of the deposited films. A valley-like curve was observed, signifying that the smoothest surface occurred at a 340 nm deposition wavelength. As the wavelength deviated from 340 nm, there was an increase in the roughness values. Specifically, the roughness values for the deposited films were 85, 53, 32, and 138 nm for lasers used with 320, 330, 340, and 350 nm wavelengths, respectively. The AFM images clearly reveal the presence of detached particles on the film surface, and their quantity and size align with the roughness trend.[31,32] In other words, the film deposited at 340 nm exhibited the fewest and smallest particles, while the film deposited at 350 nm exhibited the highest amount and largest particle size. SEM analysis further confirmed the relationship

https://doi.org/10.1021/acsomega.4c03245
ACS Omega 2024, 9, 22495−22505

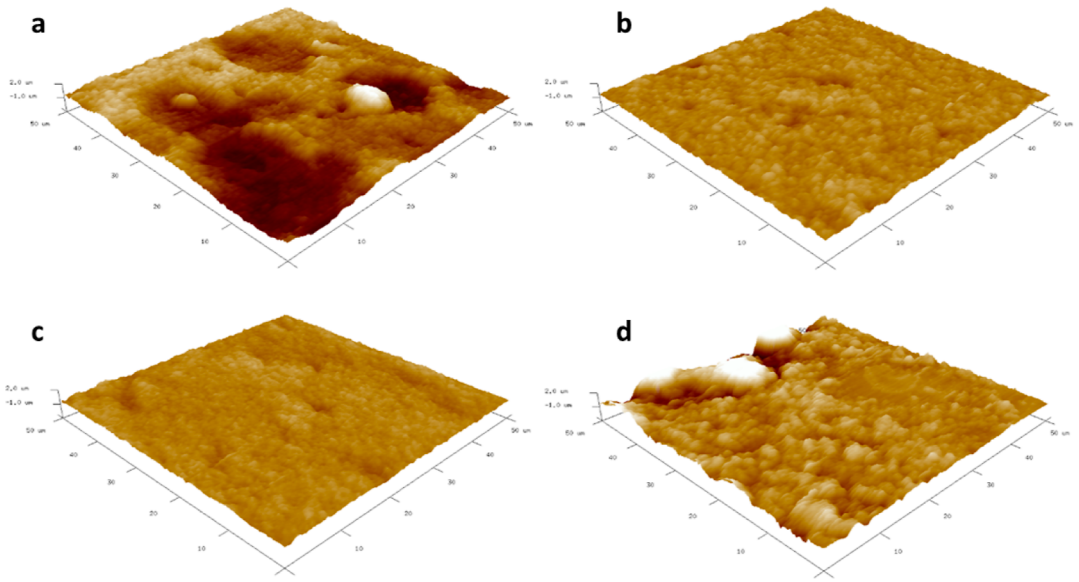


Figure 8. AFM images obtained from deposited AlCrFeMnTi films as a function of used ablation laser wavelengths (a) 320 nm, (b) 330 nm, (c) 340 nm, and (d) 350 nm

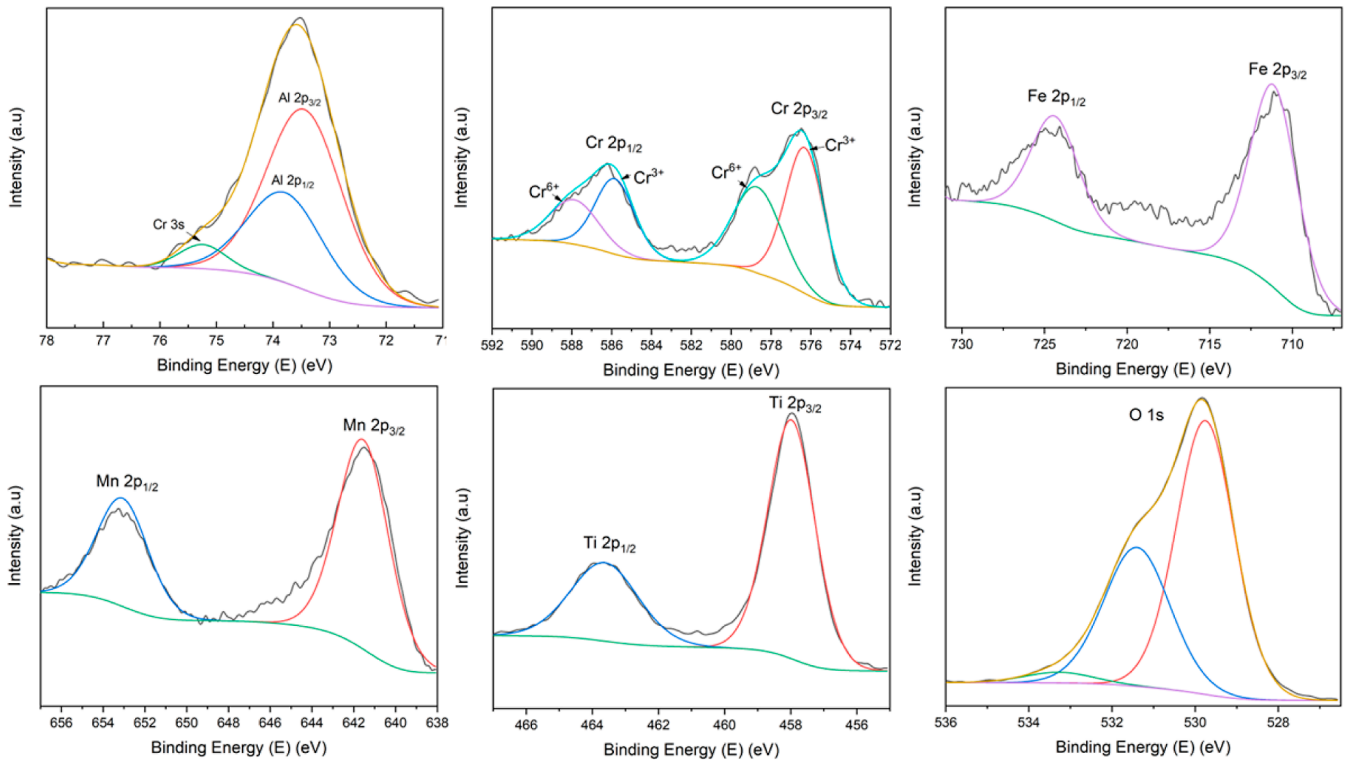


Figure 9. X-ray photoelectron spectra (XPS) analysis of AlCrFeMnTi deposited on silicon wafer by PLD at room temperature and open-air using 340 nm wavelength.

between roughness values and particle characteristics, and both methods produced consistent results. These findings provide valuable insights into the influence of the laser wavelength on the surface roughness and particle distribution of the deposited AlCrFeMnTi films.

To explain the metal and oxidation states of the elements present in the thin films deposited under various wavelengths, high-resolution XPS spectra were used, and results are presented in Figures 9 and S-2. It was focused on the Al 2p, Cr 2p, Fe 2p, Mn 2p, and Ti 2p regions. The observed Al peaks exhibited a shift of more than 1 eV toward higher binding energies compared to the position of metallic Al, which is 72.9 eV, indicating oxide formation.[33,34] Figures 9 and S-2 illustrate the presence of Al peaks in all films deposited under various wavelengths. The Al peak positions were measured as 73.64, 73.49, 73.41, and 73.48 eV for films deposited with wavelengths 350, 340, 330, and 320 nm, respectively. Additionally, the presence of Al_2O_3 peaks were detected at 74.19, 73.87, 74.01, and 74.05 eV for films deposited with laser used with wavelengths of 350, 340, 330, and 320 nm,

https://doi.org/10.1021/acsomega.4c03245
ACS Omega 2024, 9, 22495−22505

respectively, where no peak shift was detected according to the binding energy of Al_2O_3 (74.3 eV). According to these values, it can be expressed that both metallic and oxide phases of Al were observed on the film surfaces deposited under various wavelengths.[34,35] The Cr peaks in the spectrum corresponding to Cr_2O_3 and CrO_3 were detected and were expected to exhibit peaks at 576.10 and 578.30 eV, respectively. In the films deposited under different wavelengths (350, 340, 330, and 320 nm), the measured peak positions were 576.6 and 579.20 eV, 576.38 and 578.78 eV, 576.37 and 578.70 eV, and 576.57 and 578.98 eV, respectively. These values align closely with the expected binding energies, confirming that the presence of Cr_2O_3 and CrO_3 in the films are consistent with the values previously reported in the literature.[34] The high-resolution spectrum of Fe 2p shown in Figures 9 and S-2 displays two distinct peaks positioned at 711.22 and 724.59 eV, 711.27 and 724.49 eV, 711.18 and 724.58 eV, and 711.17 and 724.35 eV for the films deposited using 350, 340, 330, and 320 nm via PLD, respectively. The first peak belongs to Fe_2O_3 and the second belongs to FeO. The XPS results depicted in Figures 9 and S-2 reveal that the binding energies of Mn $2p_{3/2}$ and Mn $2p_{1/2}$ peaks are observed at 641.8 and 653.5 eV, 641.6 and 653.2 eV, 641.8 and 653.2 eV, and 641.6 and 653.2 eV, respectively, for films deposited using 350, 340, 330, and 320 nm pulsed laser wavelengths via PLD. These values closely resemble the reported outcomes in the literature, providing further evidence that the predominant oxidation states of Mn in the films are MnO_2 and Mn_2O_3.[36,37] Figures 9 and S-2 showcase a high-resolution XPS spectrum of Ti 2p, illustrating films deposited using PLD at wavelengths of 350, 340, 330, and 320 nm. The peaks observed for Ti $2p_{3/2}$ and Ti $2p_{1/2}$ in the deposited films are situated at binding energies of 458.06 and 463.74 eV, 457.98 and 463.68 eV, 457.97 and 463.62 eV, and 457.95 and 463.72 eV, respectively. Notably, the separation between the binding energies is ≈5.7 eV, which corresponds to the presence of a TiO_2 oxidation state.[32,38] The XPS analysis presented in Table 2, provides quantitative data

Table 2. Surface Oxygen and Nitrogen Composition Analysis of Coated Films Using 320, 330, 340, and 350 nm Laser Wavelengths in PLD by XPS

used laser wavelengths in PLD (nm)	320	330	340	350
O content (%)	35.53	36.27	36.23	31.92
N content (%)	0.97	1.04	0.81	0.62

on the oxygen and nitrogen content on the deposited film's surface. Nitrogen was detected in trace amounts, consistent with prior research by Atanasova et al., amounting to less than 2%.[32] The oxygen content on the films deposited with 330 and 340 nm laser wavelengths exhibited the highest oxygen content at 36.27 and 36.23%, respectively, while the lowest oxygen content, 31.92%, was observed in films deposited using a 350 nm laser wavelength.

The potentiodynamic polarization curves of the PLD-coated LWHEA specimens are shown in Figure 10. The corrosion analyses were carried out in PBS at a pH of 7.4 with a scan rate of 1 mV/s. Using the corresponding Tafel slopes of the polarization curves, the corrosion parameters were calculated as listed in Table 3. E_{corr}, I_{corr}, β_a, β_c, and R_p represent the corrosion potential, the corrosion current density, anodic Tafel slope, cathodic Tafel slope, and polarization resistance,

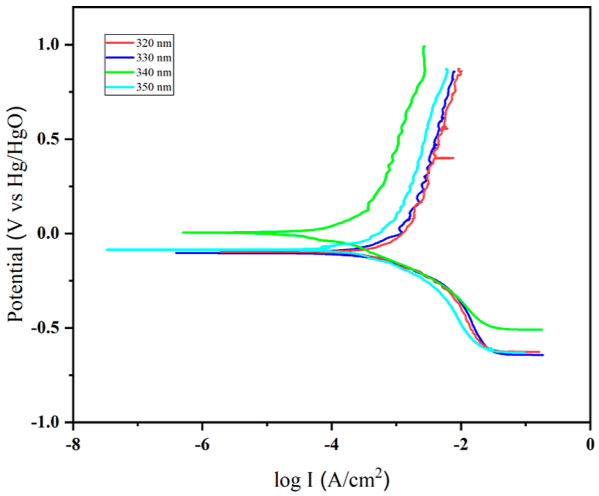


Figure 10. Potentiodynamic curves of PLD films on FTO in PBS electrolyte at a scan rate of 1 mV/s.

Table 3. Electrochemical Parameters of the LWHEA-Coated Substrates in PBS Electrolyte with a Scan Rate of 1 mV/S

	E_{corr} (mV)	I_{corr} (μA cm−2)	β_a (mV)	β_c (mV)	R_p (Ω cm²)
320 nm	−97.9	0.738	444.5	215.1	85,286
330 nm	−102	0.615	461.7	181.6	92,022
340 nm	−19.2	0.110	330.7	140.1	388,462
350 nm	−76.2	0.332	354.2	188.9	161,127

respectively. The corrosion potential is obtained from the open circuit potential (OCP), and the corrosion current density is calculated by extrapolating the linear regions of the Tafel plot near the corrosion potential. As shown in Figure 10, the coatings prepared at 340 and 350 nm are significantly smoother than those fabricated at lower wavelengths. This could be attributed to the low adhesion of the detached particles to the substrate and the coating, which emerge as horizontal lines on the potentiodynamic polarization curves in Figure 10, similar to those of pitting corrosion.

To further investigate the effects of PLD wavelengths on the corrosion resistance of the specimens, polarization resistance values were calculated using the Stern−Geary equation[39] as follows

$$I_{corr} = (\beta_a . \beta_c)/2.303(R_p(\beta_a + \beta_c)) \quad (1)$$

where β_a and β_c are calculated from the anodic and cathodic branches of the Tafel plot, respectively. According to the data represented in Table 3, the corrosion resistance of the samples increases with the wavelength at which the PLDs were performed up until 340 nm wavelengths, after which there is a decrease in the obtained polarization resistance. This behavior could be ascribed to the fact that the adhesion of the coating to the substrate is limited by the formation and separation of coarser particles at these wavelengths. Also, the more uniform microstructure and homogeneity in the film deposited at 340 nm, along with the reduced segregation minimizing the differences between grains and grain boundaries, enhance its corrosion behavior.[40] This optimum anticorrosion behavior is observed in the polarization curves where E_{corr} is the highest, I_{corr} the lowest, and consequently, R_p the highest value.

The excellent corrosion resistance of the AlCrTiFeMn HEA could be ascribed to several factors. First of all, the metallic portion of the film crystallizes in the BCC structure, which

https://doi.org/10.1021/acsomega.4c03245
ACS Omega 2024, 9, 22495−22505

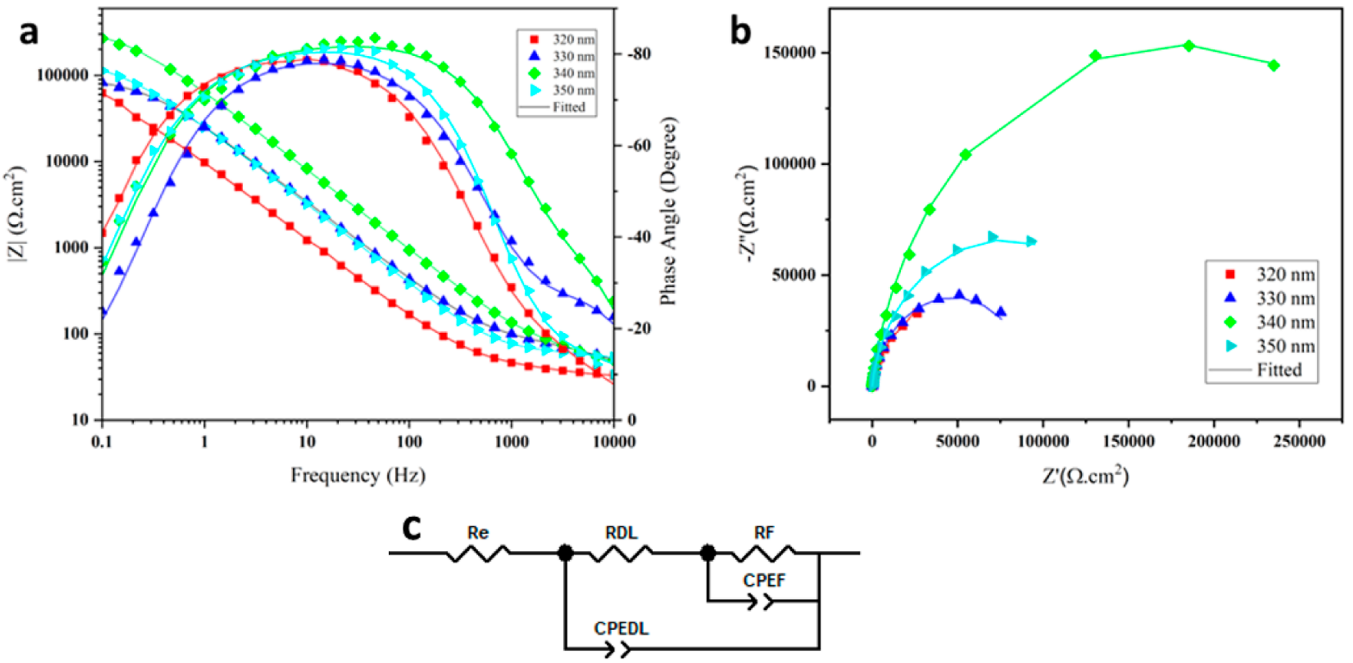


Figure 11. (a) Bode-phase and (b) Nyquist plots of LWHEA-coated FTO samples at various pulsed laser wavelengths obtained at the OCP and (c) equivalent electrical circuit used for fitting impedance data.

Table 4. Fitting Results of EIS Data Obtained at the OCP

	R_e Ω cm^2	R_{DL} Ω cm^2	CPE_{DL}-T	CPE_{DL}-P	R_{CT}	CPE_2-T	CPE_2-P
320 nm	31.7	24.7	1.4×10^{-5}	0.87	78,326	5.1×10^{-6}	0.96
330 nm	40.2	63.4	5.8×10^{-6}	0.89	93,642	1.3×10^{-6}	0.95
340 nm	42.5	58.4	2.8×10^{-6}	0.88	361,300	1.4×10^{-7}	0.95
350 nm	44.3	35.2	2.4×10^{-6}	0.88	156,770	5.2×10^{-6}	0.94

exhibits better corrosion resistance than the other cubic systems such as FCC.[41] Second, the alloy exhibits partially passive film formation in the anodic region of the polarization curve within a wide potential range, which slows down corrosion in PBS.[42] The potentiodynamic polarization curves transform directly from the Tafel region into the stable passive region, displaying that the HEO coatings are spontaneously passive at the corrosion potential.[43] This formation of a passive layer in the compound can be attributed to the presence of Al and Ti elements in the alloy. Precisely, Al improves corrosion resistance by forming a dense oxide film (Al_2O_3) and $Al(OH)_3$ in an alkaline environment, while Ti enhances the formation of protective passive films, hence increasing resistance against pitting corrosion and the overall protection effectiveness against degradation in corrosive environments.[41,44] Additionally, the strong passivation capability of Ti itself further improves the surface film, enhancing the resistance of the alloy to corrosion.[44,45]

Electrochemical impedance spectroscopy was employed to study the electrochemical processes on the surface of the LWHEA specimens during corrosion. Bode-phase and Nyquist plots of the samples at different wavelengths are shown in Figure 11a,b. The Nyquist plots emerge as depressed semicircles, the diameter of which is indicative of the corrosion resistance of the coating. Figure 11c shows the equivalent circuit data obtained by EIS. The circuit depicted in Figure 11c, consists of resistors and constant phase elements, fitted to the experimental EIS data. The equivalent circuit used for the fitting is called a nested circuit and is mainly applied when a porous or defective oxide layer is present, which exposes metallic surface areas to the electrolyte and subsequent corrosion.[46] The LWHEA structure studied in this work was of a porous nature as depicted by SEM and AFM images and also consists of a defective oxide film layer as the deposition was performed under open air conditions. In the equivalent circuit model, R_e is the Ohmic electrolyte resistance, R_{DL} represents the charge transfer resistance, CPE_{DL}-T contains the properties of the space charge layer (double layer), and R_F and CPE_F-T are the film layer resistance and film pseudo capacitance. Table 4 summarizes the parameter values acquired by fitting the EIS data. The values for electrolyte resistance are around 40 Ω cm^2 for all of the samples, as expected. The values of R_{DL} are also relatively close in a range of 20−60 Ω cm^2, and no significant difference is observed between the alloys. On the other hand, film layer resistance, R_F, varies widely between the specimens. The polarization resistance, which is the sum of R_{DL} and R_F values, is indicative of a change in the corrosion resistance and varies largely between the samples, displaying the same trend as that seen in the potentiodynamic polarization measurements. In agreement with the potentiodynamic polarization measurements, it is observed that the coating deposited at the wavelength of 340 nm shows a significantly higher resistance. This high resistance is attributed to the homogeneous dispersion and high adhesion of the coating.

https://doi.org/10.1021/acsomega.4c03245
ACS Omega 2024, 9, 22495−22505

4. CONCLUSIONS

- The LIBS analysis of the AlCrFeMnTi LWHEA revealed elemental emission peaks, providing insights into its composition and spectroscopic properties. The individual spectra obtained from elemental samples and oxygen reference peaks served as crucial reference data for understanding element behavior within the AlCrFeMnTi target.
- TEM-EDS clearly demonstrates a consistent distribution of all constituent elements and oxygen within the deposited film.
- Although a LWHEA served as the target material in the PLD process, the deposition taking place in an open-air environment resulted in the formation of both amorphous and crystalline structures. Specifically, the crystalline structure exhibited a dual-phase nature, comprising a metallic phase with a BCC structure in the $Im\bar{3}m$ (229) space group and an oxide phase with an FCC structure in the $Fd\bar{3}m$ (227) space group.
- The wavelength of the laser used in PLD significantly influences the characteristics of the deposited surface. The surfaces of the deposited films from all four wavelengths showed traces of detached particles from the target material. However, it is worth noting that when a wavelength of 340 nm was employed, the number and size of these detached particles were notably reduced compared to the other wavelengths.
- The morphology of the deposited surface was highly porous and consisted of accumulated nanoparticles, the porous nanostructures.
- The morphology of the deposited surface displayed a highly porous structure comprising accumulated nanoparticles, forming these porous nanostructures.
- The XPS surface analysis of the films deposited by PLD in an open-air environment revealed trace amounts of nitrogen, consistently measuring less than 2%. In contrast, the films displayed a significant increase in oxygen content, with the highest recorded oxygen content reaching 36.27%.
- Consistent with the findings from the potentiodynamic polarization and EIS measurements, the coating deposited at a wavelength of 340 nm demonstrates significantly higher corrosion resistance. This increased resistance is attributed to the uniform dispersion and strong adhesion of the coating.
- Based on the band gap calculation, it can be concluded that the deposited film of AlCrFeMnTi in the open air could have potential applications as a photocatalyst.

ASSOCIATED CONTENT

Supporting Information

The Supporting Information is available free of charge at https://pubs.acs.org/doi/10.1021/acsomega.4c03245.

Green compacted raw powders as pellet, X-ray photoelectron spectra (XPS) analysis of AlCrFeMnTi deposited on silicon wafer by PLD at room temperature and open air using different wavelengths, and Tauc plot of the samples calculated using the Kubelka−Munk function (PDF)

AUTHOR INFORMATION

Corresponding Author

Hadi Jahangiri − *Koç University Surface Science and Technology Center (KUYTAM), Koç University, Sariyer 34450 Istanbul, Turkey;* orcid.org/0000-0003-4403-7385; Email: hjahangiri@ku.edu.tr

Authors

Hossein Mahdavi − *Department of Materials Science and Engineering, Koç University, Sariyer 34450 Istanbul, Turkey*

Armin Asghari Alamdari − *Department of Materials Science and Engineering, Koç University, Sariyer 34450 Istanbul, Turkey;* orcid.org/0000-0002-0487-5766

Abdullah Kepceoğlu − *Koç University Surface Science and Technology Center (KUYTAM), Koç University, Sariyer 34450 Istanbul, Turkey*

M. Barış Yağcı − *Koç University Surface Science and Technology Center (KUYTAM), Koç University, Sariyer 34450 Istanbul, Turkey*

Uğur Ünal − *Koç University Surface Science and Technology Center (KUYTAM) and Department of Chemistry, Koç University, Sariyer 34450 Istanbul, Turkey;* orcid.org/0000-0003-4718-1243

Complete contact information is available at: https://pubs.acs.org/10.1021/acsomega.4c03245

Notes

The authors declare no competing financial interest.

ACKNOWLEDGMENTS

This research was generously funded by the TÜBİTAK 3501 CAREER award under project no. 122M937, as well as by TÜBİTAK through the 2218—National Postdoctoral Research Fellowship Program under project no. 118C476. We also acknowledge the support provided by TÜBİTAK under Grant no. 118C476.

REFERENCES

(1) Zhang, R. Z.; Reece, M. J. Review of High Entropy Ceramics: Design, Synthesis, Structure and Properties. *J. Mater. Chem. A* **2019**, *7* (39), 22148−22162.

(2) Justin, J. F.; Jankowiak, A. Ultra High Temperature Ceramics: Densification, Properties and Thermal Stability. *AerospaceLab J.* **2011**, *1* (3), 1−11.

(3) Bérardan, D.; Franger, S.; Meena, A. K.; Dragoe, N. Room Temperature Lithium Superionic Conductivity in High Entropy Oxides. *J. Mater. Chem. A* **2016**, *4* (24), 9536−9541.

(4) Ding, Z.; Bian, J.; Shuang, S.; Liu, X.; Hu, Y.; Sun, C.; Yang, Y. High Entropy Intermetallic-Oxide Core-Shell Nanostructure as Superb Oxygen Evolution Reaction Catalyst. *Adv. Sustainable Syst.* **2020**, *4*, 1900105.

(5) Wright, A. J.; Wang, Q.; Huang, C.; Nieto, A.; Chen, R.; Luo, J. From High-Entropy Ceramics to Compositionally-Complex Ceramics: A Case Study of Fluorite Oxides. *J. Eur. Ceram. Soc.* **2020**, *40* (5), 2120−2129.

(6) Guo, H.; Wang, X.; Dupuy, A. D.; Schoenung, J. M.; Bowman, W. J. Growth of Nanoporous High-Entropy Oxide Thin Films by Pulsed Laser Deposition. *J. Mater. Res.* **2022**, *37* (1), 124−135.

(7) Mohanty, A.; Sampreeth, J. K.; Bembalge, O.; Hascoet, J. Y.; Marya, S.; Immanuel, R. J.; Panigrahi, S. K. High Temperature Oxidation Study of Direct Laser Deposited AlXCoCrFeNi (X = 0.3, 0.7) High Entropy Alloys. *Surf. Coat. Technol.* **2019**, *380* (October), 125028.

(8) Cai, Z.; Cui, X.; Jin, G.; Liu, Z.; Zheng, W.; Li, Y.; Wang, L. Microstructure and Thermal Stability of a Ni-Cr-Co-Ti-V-Al High-

Entropy Alloy Coating by Laser Surface Alloying. *Met. Mater. Int.* **2017**, *23* (5), 1012−1018.
(9) Tunes, M. A.; Vishnyakov, V. M. Microstructural Origins of the High Mechanical Damage Tolerance of NbTaMoW Refractory High-Entropy Alloy Thin Films. *Mater. Des.* **2019**, *170*, 107692.
(10) Braic, V.; Vladescu, A.; Balaceanu, M.; Luculescu, C. R.; Braic, M. Nanostructured Multi-Element (TiZrNbHfTa)N and (TiZrNbHf-Ta)C Hard Coatings. *Surf. Coat. Technol.* **2012**, *211*, 117−121.
(11) Laszlo, E. A.; Crăciun, D.; Dorcioman, G.; Crăciun, G.; Geantă, V.; Voiculescu, I.; Cristea, D.; Crăciun, V. Characteristics of Thin High Entropy Alloy Films Grown by Pulsed Laser Deposition. *Coatings* **2022**, *12* (8), 1211.
(12) Cropper, M. D. Thin Films of AlCrFeCoNiCu High-Entropy Alloy by Pulsed Laser Deposition. *Appl. Surf. Sci.* **2018**, *455*, 153−159.
(13) Asghari Alamdari, A.; Hashemkhani, M.; Hendessi, S.; Yagci Acar, H.; Unal, U.; Motallebzadeh, A. A comprehensive study of microstructure, mechanical behavior, biocorrosion, and cytotoxicity of RF-PVD deposited Ti1.5ZrTa0.5Nb0.5X0.5 (X: Hf, Mo, and W) refractory high-entropy alloy films on 316L. *Intermetallics* **2023**, *162*, 108003.
(14) Salian, A.; Mandal, S. Review on the Deposition, Structure and Properties of High Entropy Oxide Films: Current and Future Perspectives. *Bull. Mater. Sci.* **2022**, *45* (1), 49−21.
(15) Shepelin, N. A.; Tehrani, Z. P.; Ohannessian, N.; Schneider, C. W.; Pergolesi, D.; Lippert, T. A Practical Guide to Pulsed Laser Deposition. *Chem. Soc. Rev.* **2023**, *52* (7), 2294−2321.
(16) Guo, H.; Wang, X.; Dupuy, A. D.; Schoenung, J. M.; Bowman, W. J. Growth of Nanoporous High-Entropy Oxide Thin Films by Pulsed Laser Deposition. *J. Mater. Res.* **2022**, *37* (1), 124−135.
(17) Craciun, D.; Laszlo, E. A.; Mirza-Rosca, J. C.; Dorcioman, G.; Geanta, V.; Voiculescu, I.; Craciun, G.; Badea, L.; Craciun, V. Structural Parameters and Behavior in Simulated Body Fluid of High Entropy Alloy Thin Films. *Materials* **2024**, *17* (5), 1162.
(18) Jung, S.-G.; Han, Y.; Kim, J. H.; Hidayati, R.; Rhyee, J.-S.; Lee, J. M.; Kang, W. N.; Choi, W. S.; Jeon, H.-R.; Suk, J.; Park, T. High Critical Current Density and High-Tolerance Superconductivity in High-Entropy Alloy Thin Films. *Nat. Commun.* **2022**, *13* (1), 3373.
(19) Nikov, R. G.; Dikovska, A. O.; Nedyalkov, N. N.; Atanasov, P. A.; Atanasova, G.; Hirsch, D.; Rauschenbach, B. ZnO Nanostructures Produced by Pulsed Laser Deposition in Open Air. *Appl. Phys. A Mater. Sci. Process.* **2017**, *123* (10), 657−7.
(20) Białous, A.; Gazda, M.; Grochowska, K.; Atanasov, P.; Dikovska, A.; Nedyalkov, N.; Reszczyńska, J.; Zaleska-Medynska, A.; Śliwiński, G. Nanoporous TiO2 Electrode Grown by Laser Ablation of Titanium in Air at Atmospheric Pressure and Room Temperature. *Thin Solid Films* **2016**, *601*, 41−44.
(21) Mohamed, W. T. Y. Improved LIBS Limit of Detection of Be, Mg, Si, Mn, Fe and Cu in Aluminum Alloy Samples Using a Portable Echelle Spectrometer with ICCD Camera. *Opt. Laser Technol.* **2008**, *40* (1), 30−38.
(22) Cheng, M.-D. Real-Time Measurement of Trace Metals on Fine Particles by Laser-Induced Plasma Techniques. *Fuel Process. Technol.* **2000**, *65*−*66*, 219−229.
(23) Shirai, T.; Reader, J.; Kramida, A. E.; Sugar, J. *NIST ASD Team. {NIST} {Atomic} {Spectra} {Database} (Ver.~5.0)*. Mem. SA It. Suppl., 2012; pp 96−102.
(24) Tran, M.; Sun, Q.; Smith, B. W.; Winefordner, J. D. Determination of C: H: O: N Ratios in Solid Organic Compounds by Laser-Induced Plasma Spectroscopy. *J. Anal. At. Spectrom.* **2001**, *16* (6), 628−632.
(25) Bassim, N. D.; Schenck, P. K.; Donev, E. U.; Heilweil, E. J.; Cockayne, E.; Green, M. L.; Feldman, L. C. Effects of Temperature and Oxygen Pressure on Binary Oxide Growth Using Aperture-Controlled Combinatorial Pulsed-Laser Deposition. *Appl. Surf. Sci.* **2007**, *254*, 785−788.
(26) Chen, J.; Huang, R.; Zhou, X.; Zhou, D.; Li, M.; Bai, C.; Liu, Z.; Cai, C. Nucleation and Epitaxy Growth of High-Entropy REBa2Cu3O7- (RE= Y, Dy, Gd, Sm, Eu) Thin Films by Metal Organic Deposition. *J. Rare Earths* **2023**, *41* (7), 1091−1098.
(27) Chen, J.; Ling, Y.; Yu, X.; Wang, G.; Huang, L.; He, A.; Fan, Q.; Qin, S.; Xiang, S.; Xu, M.; Han, Z.; Du, J.; Xu, Q. Water Oxidation on CrMnFeCoNi High Entropy Alloy: Improvement through Rejuvenation and Spin Polarization. *J. Alloys Compd.* **2022**, *929*, 167344.
(28) Koralli, P.; Petropoulou, G.; Mouzakis, D. E.; Mousdis, G.; Kompitsas, M. Efficient CO Sensing by a CuO:Au Nanocomposite Thin Film Deposited by PLD on a Pyrex Tube. *Sens. Actuators, A* **2021**, *332*, 113120.
(29) Chen, Z. W.; Lai, J. K. L.; Shek, C. H.; Chen, H. D. Production of Amorphous Tin Oxide Thin Films and Microstructural Transformation Induced by Heat Treatment. *Appl. Phys. A: Mater. Sci. Process.* **2005**, *81* (5), 1073−1076.
(30) Yamaki, T.; Sumita, T.; Yamamoto, S.; Miyashita, A. Preparation of Epitaxial TiO2 Films by PLD for Photocatalyst Applications. *J. Cryst. Growth* **2002**, *237*−*239* (1−4 I), 574−579.
(31) Sanz, M.; Walczak, M.; Oujja, M.; Cuesta, A.; Castillejo, M. Nanosecond Pulsed Laser Deposition of TiO2: Nanostructure and Morphology of Deposits and Plasma Diagnosis. *Thin Solid Films* **2009**, *517* (24), 6546−6552.
(32) Atanasova, G.; Dikovska, A. O.; Dilova, T.; Georgieva, B.; Avdeev, G. V.; Stefanov, P.; Nedyalkov, N. N. Metal-Oxide Nanostructures Produced by PLD in Open Air for Gas Sensor Applications. *Appl. Surf. Sci.* **2019**, *470* (November 2018), 861−869.
(33) Evans, H. E.; Bowser, W. M.; Weinberg, W. H. An XPS Investigation of Alumina Thin Films Utilized in Inelastic Electron Tunneling Spectroscopy. *Appl. Surf. Sci.* **1980**, *5* (3), 258−274.
(34) Khan, N. A.; Akhavan, B.; Zhou, H.; Chang, L.; Wang, Y.; Sun, L.; Bilek, M. M.; Liu, Z. High Entropy Alloy Thin Films of AlCoCrCu0.5FeNi with Controlled Microstructure. *Appl. Surf. Sci.* **2019**, *495*, 143560.
(35) Djebaili, K.; Mekhalif, Z.; Boumaza, A.; Djelloul, A. XPS, FTIR, EDX, and XRD Analysis of Al 2 O 3 Scales Grown on PM2000 Alloy. *J. Spectrosc.* **2015**, *2015*, 1−16.
(36) Zhou, T.; Zhao, Y.; Chen, H.; Du, X.; Chen, W.; Dong, Z.; Wang, X.; Shen, J.; Wu, Z.; Liu, W.; Zhang, Y. Self-Recoverable near-Infrared Mechanoluminescence from ZnS:Mn by Controlling Manganese Clusterization. *Mater. Des.* **2022**, *224*, 111407.
(37) Biesinger, M. C.; Payne, B. P.; Grosvenor, A. P.; Lau, L. W. M.; Gerson, A. R.; Smart, R. S. C. Resolving Surface Chemical States in XPS Analysis of First Row Transition Metals, Oxides and Hydroxides: Cr, Mn, Fe, Co and Ni. *Appl. Surf. Sci.* **2011**, *257* (7), 2717−2730.
(38) Biesinger, M. C.; Lau, L. W. M.; Gerson, A. R.; Smart, R. S. C. Resolving Surface Chemical States in XPS Analysis of First Row Transition Metals, Oxides and Hydroxides: Sc, Ti, V, Cu and Zn. *Appl. Surf. Sci.* **2010**, *257* (3), 887−898.
(39) Stern, M.; Geaby, A. L.; Banjade, D. R.; Porter, S. D.; McMullan, B. M.; Koleva, D. A.; de Wit, J. H.; van Breugel, K. Electrochemical Polarization: I. A Theoretical Analysis of the Shape of Polarization Curves. *J. Electrochem. Soc.* **1957**, *104* (1), 56.
(40) Qiu, X.; Wu, M.; Liu, C.; Zhang, Y.; Huang, C. Corrosion Performance of Al2CrFeCoxCuNiTi High-Entropy Alloy Coatings in Acid Liquids. *J. Alloys Compd.* **2017**, *708*, 353−357.
(41) Sünbül, S. E.; İçin, K.; Şeren, F. Z.; Şahin, O.··; Çakil, D. D.; Sezer, R.; Öztürk, S. Determination of Structural, Tribological, Isothermal Oxidation and Corrosion Properties of Al-Co-Cr-Fe-Ni-Ti-Cu High-Entropy Alloy. *Vacuum* **2021**, *187*, 110072.
(42) Wu, C. L.; Zhang, S.; Zhang, C. H.; Zhang, H.; Dong, S. Y. Phase Evolution and Cavitation Erosion-Corrosion Behavior of FeCoCrAlNiTix High Entropy Alloy Coatings on 304 Stainless Steel by Laser Surface Alloying. *J. Alloys Compd.* **2017**, *698*, 761−770.
(43) Ma, G.; Zhao, Y.; Cui, H.; Song, X.; Wang, M.; Lee, K.; Gao, X.; Song, Q.; Wang, C. Addition Al and/or Ti Induced Modifications of Microstructures, Mechanical Properties, and Corrosion Properties in CoCrFeNi High-Entropy Alloy Coatings. *Acta Metall. Sin.* **2021**, *34* (8), 1087−1102.
(44) Fu, Y.; Li, J.; Luo, H.; Du, C.; Li, X. Recent Advances on Environmental Corrosion Behavior and Mechanism of High-Entropy Alloys. *J. Mater. Sci. Technol.* **2021**, *80*, 217−233.

https://doi.org/10.1021/acsomega.4c03245
ACS Omega 2024, 9, 22495−22505

(45) Wu, M.; Setiawan, R. C.; Li, D. Y. Benefits of Passive Element Ti to the Resistance of AlCrFeCoNi High-Entropy Alloy to Corrosion and Corrosive Wear. *Wear* **2022**, *492−493*, 204231.
(46) Zemanate, A. M.; Jorge Júnior, A. M.; Andreani, G. F. d. L.; Roche, V.; Cardoso, K. R. Corrosion Behavior of AlCoCrFeNix High Entropy Alloys. *Electrochim. Acta* **2023**, *441*, 141844.

https://doi.org/10.1021/acsomega.4c03245
ACS Omega 2024, 9, 22495−22505